A modified 3D-2D convolutional neural networks for robust mineral identification: Hyperspectral analysis in Djebel Meni (Northwestern Algeria)

Youcef Attallah, Ehlem Zigh, Zoulikha Mehalli and Adda Ali Pacha

Laboratory of Coding and Security of Information, University of Sciences and Technology of Oran Mohamed Boudiaf, PO Box 1505, Oran M'Naouer 31000, Algeria

Abstract

This study explores the use of an optimized 3D-2D convolutional neural network (CNN) model for effective mineral identification in the Djebel Meni region of Northwestern Algeria, utilizing hyperspectral imaging data from NASA's Hyperion EO-1 sensor. Given the challenges posed by remote, complex geological terrains, our approach integrates advanced deep-learning techniques with hyperspectral data to enhance mineral classification accuracy. Following atmospheric correction using the Quac module, spectral signatures of the target minerals—illite, kaolinite, and montmorillonite—from the United States Geological Survey (USGS) spectral library were employed as reference inputs. By leveraging this corrected hyperspectral data, the 3D-2D CNN model was trained to classify these clay minerals with high precision, achieving an overall accuracy of 94.26% and an average class-specific accuracy of 93.93%. These results highlight the model's robustness in differentiating mineral compositions in geologically challenging contexts, even when limited ground truth data is available. This research underscores the potential of combining hyperspectral remote sensing with sophisticated CNN architectures to advance mineral identification and geospatial analysis, offering valuable insights for mineralogical studies in similar remote regions.

Keywords

Hyperspectral Imaging, 3D-2D CNN, Mineral Identification, USGS Spectral Library, Djebel Meni

1. Introduction

Identifying and classifying minerals in remote and geologically complex terrains is a formidable challenge, especially in hard-to-access regions. Traditional field-based mineral identification methods are often limited due to high costs, time constraints, and logistical barriers, which restrict the collection of comprehensive data across extensive areas [1]. Hyperspectral imaging (HSI) has emerged as a powerful remote sensing tool, addressing these limitations by enabling detailed mineral identification and classification through spectral analysis. By capturing unique spectral signatures associated with various minerals, HSI facilitates high-resolution mapping of mineral compositions over vast and difficult-to-reach landscapes, significantly reducing the need for direct physical sampling [2].

NASA's launch of the EO-1 Hyperion sensor in November 2000 marked a new era in spaceborne hyperspectral mapping capabilities, transforming the field of remote mineral exploration. The Hyperion sensor provides a spectral range of 0.4 to 2.5 μm across 242 spectral bands with a spectral resolution of approximately 10 nm and a spatial resolution of 30 meters, making it highly suited for geological studies [3]. With dual spectrometers covering the visible/near-infrared (VNIR) and short-wave infrared (SWIR) regions, Hyperion has been extensively used to map mineral distributions on Earth's surface, even in challenging and rugged terrains. Numerous studies have leveraged Hyperion data for mineralogical applications, developing and refining methods to retrieve detailed mineralogical information from hyperspectral data [4, 5, 6, 7]. By providing a reliable and scalable approach, Hyperion offers a unique

CS&SE@SW 2024: 7th Workshop for Young Scientists in Computer Science & Software Engineering, December 27, 2024, Kryvyi Rih, Ukraine

youcef.attallah@univ-usto.dz (Y. Attallah); ehlem.zigh@univ-usto.dz (E. Zigh); zoulikha.mehalli@univ-usto.dz (Z. Mehalli); a.alipacha@gmail.com (A. Ali Pacha)

0000-0003-2623-7412 (Y. Attallah); 0000-0002-4161-8582 (E. Zigh); 0009-0002-7442-9400 (Z. Mehalli); 0000-0003-1828-9562 (A. Ali Pacha)

opportunity to detect subtle spectral differences that reveal the presence of various minerals, even in mineral-rich yet hard-to-access regions [8].

With the rapid advancement of artificial intelligence, deep learning models have proven particularly effective in analyzing the high-dimensional datasets generated by hyperspectral imaging [9]. While previous studies have primarily applied convolutional neural networks (CNNs), including hybrid 3D-2D CNN architectures, to domains such as vegetation analysis, this work extends their application to mineral classification, addressing a significant gap in the literature. Our approach introduces a novel 3D-2D CNN architecture specifically designed for the unique challenges of mineral mapping in hyperspectral data. Unlike prior methods, which focus on traditional classification approaches such as the spectral angle mapper (SAM) or machine learning models, our hybrid architecture leverages the strengths of 3D convolutions to extract detailed spectral features and 2D convolutions to capture spatial patterns, resulting in superior classification performance [10].

In this study, we aim to develop and evaluate an optimized 3D-2D CNN model for the precise classification of clay minerals—illite, kaolinite, and montmorillonite—using hyperspectral imaging data from the Djebel Meni region in Algeria. The primary objective is to demonstrate that the hybrid combination of 3D and 2D convolutional operations can effectively capture hyperspectral data's spectral and spatial features, thereby improving classification performance. To ensure the reliability of our results, validated mineral classifications derived from the spectral information divergence (SID) method and the USGS spectral library were used as ground truth [11]. The hyperspectral data was preprocessed with the QUAC module for atmospheric correction to enhance data quality further [12]. This study highlights the capability of deep learning in addressing the challenges of mineral classification in geologically complex terrains and establishes a reproducible framework for applying hybrid CNN models in remote mineral exploration.

The remainder of this paper is structured as follows: Section 2 presents the study area and materials, detailing the region and hyperspectral datasets used. Section 3 describes the methodology, focusing on the data preprocessing, SID validation, and CNN architecture. Section 4 discusses the results, including classification accuracy and comparative analysis, and section 5 concludes with insights into the implications of our findings and potential directions for future research.

2. Study area and materials

2.1. Study area

The study area is located in Northwestern Algeria, between latitudes $36°04'28.06''$ and $36°03'45.11''N$ and longitudes $0°23'15.02''$ and $0°31'08.59''E$. It spans approximately $125\ km^2$, with an average elevation between 100 and 200 meters. The climate is semi-arid, with annual rainfall averaging around 350 mm. Geologically, the region is largely composed of claystone formations, making it suitable for mineralogical research, particularly for the study of minerals like illite, kaolinite, and montmorillonite [3, 13].

Djebel Meni, a hill in the Atlas Mountains, reaches an elevation of 313 meters ($1,027$ feet) with a prominence of 171 meters (561 feet). The site includes small open-pit mines and quarries for bentonite extraction, emphasizing its economic and geological significance. The availability of hyperspectral imagery from the Hyperion sensor also contributed to the selection of this area, facilitating remote mineral identification and geological mapping [14].

Figure 1 provides a visual overview of the study area; the left panel shows the geological map of Hadjadj (ex. Bosquet) based on Jacob's 1902 survey, illustrating various formations, including Helvetian clays and sandstone; the right panel displays the area on Google Earth, indicating key landmarks like Djebel Meni and surrounding features.

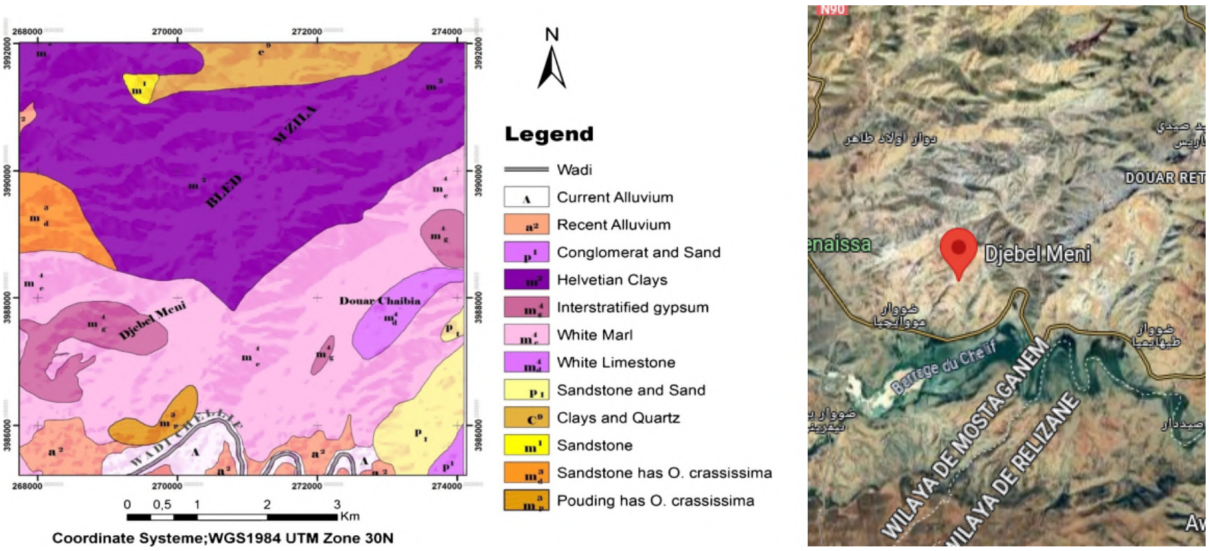

Figure 1: Location and geological map of the Djebel Meni study area, north-west Algeria [3].

2.2. Hyperion data

This study uses data from the Hyperion sensor aboard the EO-1 satellite, launched by NASA on November 21, 2000. The satellite orbits the Earth at an altitude of 705 km and passes over the same regions at the same local time, allowing for consistent comparisons.

The Hyperion sensor captures light reflected from the Earth's surface using two spectrometers:

- VNIR (Visible and Near-Infrared): Measures wavelengths from 0.355 μm to 1 μm across 70 spectral bands.
- SWIR (Short-Wave Infrared): Measures wavelengths from 0.9 μm to 2.5 μm across 172 spectral bands.

Hyperion records 242 spectral bands with a 10 nm interval between them. The images have a spatial resolution of 30 m, enabling detailed soil and rock composition analysis in small areas [15].

The specific data used in this study has the following characteristics:

- **Acquisition date:** December 17, 2010
- **Spatial resolution:** 30 m
- **Spectral resolution:** 10 nm
- **Number of bands:** 242

Thanks to its high spectral resolution, Hyperion data allows for the identification of specific mineral signatures, such as illite, kaolinite, and montmorillonite, even in geologically complex areas like Djebel Meni [13].

3. Methodology

The proposed methodology aims to efficiently process hyperspectral data and extract valuable geological insights through a series of well-defined steps. As illustrated in figure 2, the process begins with data preprocessing, which includes essential corrections such as bad bands removal to eliminate noisy and irrelevant spectral information, radiometric calibration to address sensor-induced distortions, and atmospheric correction to reduce the impact of atmospheric interference. Following preprocessing, dimensionality reduction is performed using principal component analysis (PCA) to simplify the dataset while preserving key spectral features. The next step involves image segmentation through the SID method, which isolates distinct mineralogical zones within the hyperspectral image. Subsequently,

data modeling is carried out using a combination of 3D and 2D CNNs to analyze and classify the data effectively. Finally, the methodology concludes with evaluation and comparisons, where the results are assessed, and the proposed approach is benchmarked against other techniques to validate its performance and reliability. The workflow is designed to ensure an accurate and comprehensive analysis of hyperspectral data.

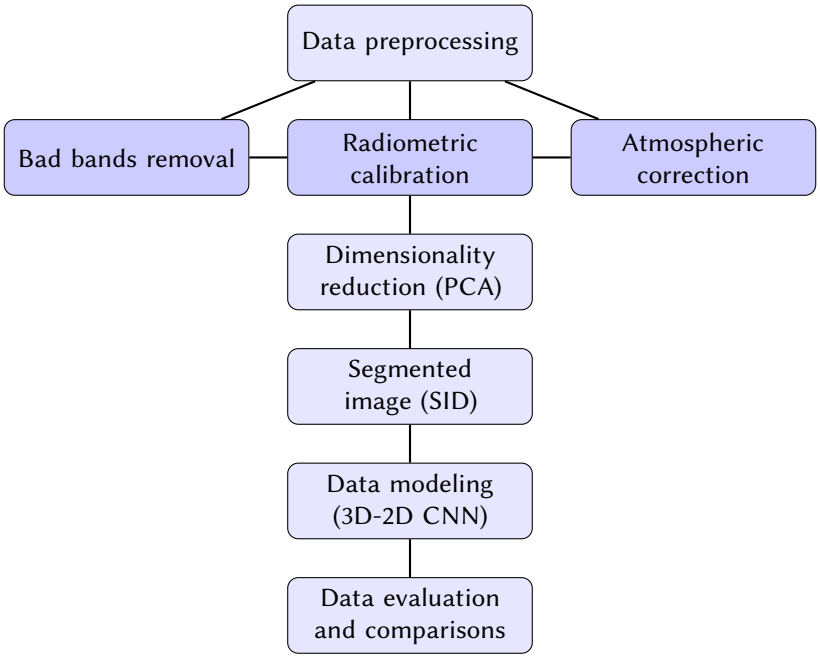

Figure 2: Flowchart of the proposed 3D-2D CNN for mineral identification in hyperspectral images.

3.1. Data preprocessing

3.1.1. Bad bands removal

Data preprocessing is crucial in hyperspectral image analysis, ensuring the data is clean and reliable for further processing. One essential task in this phase is bad band removal (BBR), which focuses on identifying and excluding spectral bands affected by noise, sensor artefacts, or atmospheric interference [16]. Certain wavelength ranges are particularly susceptible to absorption by atmospheric gases, which reduces their quality:

- **Water vapor (H_2O):** Strong absorption occurs around $1.4\ \mu m$ and $1.9\ \mu m$, excluding bands in these regions.
- **Carbon dioxide (CO_2):** Affects the spectral range near $2\ \mu m$, specifically from $1.95\ \mu m$ to $2.05\ \mu m$.
- **Ozone (O_2):** Impacts the VNIR region below $0.4\ \mu m$, where the signal is weak and noisy.

This study identified bad bands through spectral analysis, removed them from the dataset, and verified them to ensure that only relevant spectral information was retained. Table 1 summarizes the bands removed, their corresponding spectrometer, wavelength ranges, and reasons for exclusion.

3.1.2. Radiometric calibration

Hyperspectral images acquired by the Hyperion EO-1 sensor contain closely spaced spectral bands, which can introduce radiometric errors. Radiometric, geometric, and atmospheric correction is required to ensure accurate use of the data [17]. Radiometric calibration converts raw pixel values into physical

Table 1
Summary of bad band removal in the preprocessing phase.

Bands	Spectrometer	Wavelength (µm)	Situation
1–7	VNIR	0.35–0.41	Removed
8–57	VNIR	0.42–0.88	Accepted
58–70	VNIR	0.89–0.95	Removed
71–99	SWIR	0.95–1.13	Removed
100–120	SWIR	1.14–1.34	Accepted
121–134	SWIR	1.35–1.48	Removed
135–164	SWIR	1.49–1.79	Removed
165–190	SWIR	1.80–2.05	Removed
191–224	SWIR	2.06–2.39	Accepted
225–242	SWIR	2.40–2.57	Removed

units of luminance, and atmospheric correction is essential to eliminate atmospheric effects and transform data into surface reflectance values. Radiometric calibration was performed using the following equation:

$$L_\lambda = \text{gain} \cdot \text{pixel value} + \text{offset} \tag{1}$$

where L_λ represents the luminance at a specific wavelength (λ), the gain factor corresponds to the amplification of the signal during the analog-to-digital conversion (ADC) process, and the offset factor compensates for any systematic bias in the sensor response. The raw pixel value translates the electrical signal measured by the corresponding detector at each position in the image [18, 17].

3.1.3. Atmospheric correction

Radiometric calibration and atmospheric correction are essential steps in processing hyperspectral data, as atmospheric conditions significantly influence remote sensing measurements. Scattering and absorption by atmospheric gases and particulates alter the light reaching the sensor, with water vapour being the primary contributor, followed by gases such as carbon dioxide and ozone [19]. The Hyperion data was atmospherically corrected in this study using the quick atmospheric correction (QUAC) module.

QUAC determines atmospheric parameters directly from the observed pixel spectra in the image without requiring external information. While it is less precise than physics-based methods like FLAASH, QUAC typically produces 'reflectance spectra, which measure the proportion of incident light reflected by a surface, with an accuracy of about 10% relative to ground truth [20]. The final output of atmospheric correction is the reflectance spectrum, which measures the proportion of sunlight reflected by a surface. This spectrum is essential for identifying and classifying surface materials, as it removes the atmospheric effects that can obscure true spectral signatures. By combining radiometric calibration and atmospheric correction, the Hyperion data were standardized, enabling accurate analysis and interpretation of spectral information for geological applications.

3.2. Dimensionnality reduction

For the classification of hyperspectral images in the Djebel Meni region (Northwestern Algeria) using Hyperion EO-1 data, dimensionality reduction is a crucial preprocessing step. Instead of relying on methods like PCA, we reduced the number of spectral bands to 30 by selecting those containing the most valuable information for classifying the three minerals of interest: Illite, Kaolinite, and Montmorillonite. This targeted band selection preserves critical features for classification while discarding redundant or less informative bands, optimizing the dataset for subsequent analysis.

By integrating this reduced dataset into the 3D-2D CNN architecture, we ensured efficient computation, faster model convergence, and improved classification accuracy. This approach enhances the network's ability to extract and analyze meaningful spectral-spatial features relevant to the identification of the selected minerals [21].

3.3. Data segmentation

The segmentation process is a critical step in hyperspectral image analysis. It aims to identify and isolate specific mineral signatures within the hyperspectral data by dividing the image into distinct regions corresponding to different mineral classes. This step is essential for highly precisely classifying and mapping minerals in complex geological environments.

This study employs the *spectral information divergence (SID)* algorithm as the primary segmentation tool. SID is widely recognized for its robustness in detecting spectral variations by measuring the divergence between the spectral signature of each pixel and reference spectra. Unlike simpler methods such as spectral angle mapper (SAM), SID accounts for subtle spectral differences, making it particularly effective for identifying minerals with overlapping spectral features [22].

The SID algorithm operates as follows:

- **Input spectral data:** Each pixel in the hyperspectral image contains a spectrum representing the reflectance values at multiple wavelengths.
- **Reference spectra:** Spectral signatures from the USGS library are reference inputs for illite, kaolinite, and montmorillonite.
- **Comparison:** SID calculates the divergence between each pixel's spectrum and the reference spectra. Lower divergence values indicate a higher likelihood that the pixel belongs to a specific mineral class.

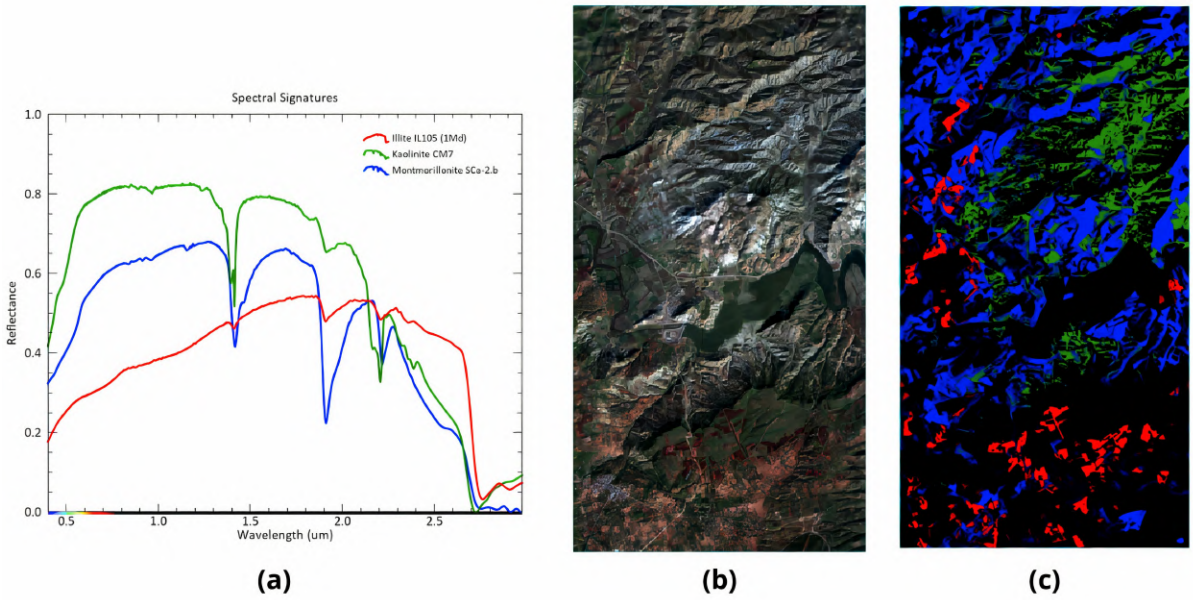

Figure 3: Spectral signatures and ground truth segmentation of the Djebel Meni hyperspectral image.

As illustrated in digure 3, the segmentation process can be divided into three main components:

- **Spectral signatures** (figure 3.a): The unique reflectance patterns of illite, kaolinite, and montmorillonite are extracted from the USGS dataset. These patterns serve as the basis for segmentation, as each mineral exhibits distinct spectral characteristics in specific wavelength ranges.
- **Input hyperspectral image** (figure 3.b): The preprocessed hyperspectral image serves as the input to the SID algorithm. It contains all spectral bands retained after preprocessing, such as bad band removal and atmospheric correction.
- **Segmented map** (figure 3.c): The output of the SID algorithm is a segmented map where a distinct colour represents each mineral class:
  - **Red:** Illite

  - **Green:** Kaolinite
  - **Blue:** Montmorillonite

The segmented map includes pixel samples for each mineral class, which serve as ground truth for model evaluation. The number of pixels assigned to each class is as follows:

- **Illite:** 4,775 pixels
- **Kaolinite:** 12,042 pixels
- **Montmorillonite:** 24,410 pixels

This segmentation process enables precise mineral identification by leveraging the high spectral resolution of Hyperion data and the advanced capabilities of the SID algorithm.

3.4. Data modeling

Our study introduces a hybrid convolutional neural network (CNN) architecture aimed at classifying minerals from the Djebel Meni region. This approach leverages a 3D-2D CNN framework designed to effectively capture both spatial and spectral features inherent in hyperspectral imagery. The architecture incorporates four 3D convolutional layers tailored to extract spatial and spectral details. Specifically, the kernel sizes for these layers are defined as follows:

- **First layer:** $8 \times 3 \times 3 \times 3 \times 1$ ($F_1^1 = 3, F_2^1 = 3, F_3^1 = 3$).
- **Second layer:** $16 \times 3 \times 3 \times 3 \times 8$ ($F_1^2 = 3, F_2^2 = 3, F_3^2 = 3$).
- **Third layer:** $16 \times 3 \times 3 \times 3 \times 16$ ($F_1^3 = 3, F_2^3 = 3, F_3^3 = 3$).
- **Fourth layer:** $32 \times 3 \times 3 \times 3 \times 16$ ($F_1^4 = 3, F_2^4 = 3, F_3^4 = 3$).

The 2D segment of the model consists of three 2D convolutional layers with the following kernel configurations:

- **First layer:** $32 \times 3 \times 3 \times 32$ ($F_1^1 = 3, F_2^1 = 3$).
- **Second layer:** $16 \times 3 \times 3 \times 32$ ($F_1^2 = 3, F_2^2 = 3$).
- **Third layer:** $8 \times 3 \times 3 \times 16$ ($F_1^3 = 3, F_2^3 = 3$).

The output from the seventh layer is flattened, and all neurons are fully connected to the next layer with 64 neurons, culminating in a classification layer that outputs predictions for 3 mineral classes. A detailed summary of the model, including layer types, output dimensions, and parameter counts, is provided in table 2. Notably, the initial dense layer contains the highest number of parameters, and the total parameter count for the model depends on the number of classes in the dataset. For the hyperspectral dataset, the proposed model includes $301,947$ trainable parameters.

Extensive experimental evaluations to optimize the classification of minerals in hyperspectral images drove the choice of the hybrid 3D-2D CNN architecture. This architecture demonstrated superior performance, particularly in mineral-rich regions such as Cuprite, due to its ability to efficiently extract spatial and spectral features. Specifically, the 3D convolutional layers effectively capture spectral dependencies, while the 2D layers enhance spatial feature representation, improving classification accuracy.

The number of layers and filter sizes was carefully determined based on iterative testing to balance computational complexity and classification performance. For instance, smaller kernel sizes in the 3D layers ensured precise spectral feature extraction, while larger kernel sizes in the 2D layers improved the spatial generalization of mineral patterns. The proposed design was validated on diverse hyperspectral datasets, confirming its robustness and applicability for mineral identification tasks [9]. This hybrid approach leverages the strengths of both 3D and 2D convolutions:

1. **3D convolutions for spectral-spatial features:** The initial 3D layers capture spectral-spatial correlations by simultaneously analyzing the spatial and spectral dimensions of the hyperspectral images. This is particularly critical for hyperspectral data, as the spectral signatures play a vital role in identifying mineral types.

2. **2D convolutions for spatial refinement:** The subsequent 2D layers focus on refining spatial features after the 3D layers adequately encode the spectral information. This separation of tasks ensures efficient feature extraction and reduces computational complexity.
3. **Filter sizes and layer depth:** Experiments guided the choice of kernel sizes (e.g., 3x3x3 for 3D layers) to balance the trade-off between capturing fine-grained details and maintaining computational efficiency. Smaller kernel sizes allowed the network to focus on local interactions while ensuring a sufficient depth of representation across layers.

The model's weights are initialized randomly and optimized using the backpropagation algorithm with the Adam optimizer. Softmax activation is employed for classification purposes. The network is trained over 100 epochs with a batch size of 256 samples and a learning rate of 0.001 without employing data augmentation techniques. This hybrid CNN effectively captures the spatial and spectral richness of hyperspectral images, utilizing 3D convolutions to harness spectral depth and 2D convolutions to refine spatial features.

Table 2
Summary of the architecture of the proposed 3D-2D convolutional neural network.

Layer	Output shape	Parameters
Input layer	(25, 25, 30, 1)	0
Conv3D 1 (Conv3D)	(23, 23, 28, 8)	224
Conv3D 2 (Conv3D)	(21, 21, 26, 16)	3472
Conv3D 3 (Conv3D)	(19, 19, 24, 16)	6928
Conv3D 4 (Conv3D)	(17, 17, 22, 32)	13856
Reshape 1 (Reshape)	(17, 17, 704)	0
Batch normalization 1	(17, 17, 704)	2816
Conv2D 1 (Conv2D)	(15, 15, 32)	202784
Conv2D 2 (Conv2D)	(13, 13, 16)	4624
Conv2D 3 (Conv2D)	(11, 11, 8)	1160
Flatten (Flatten)	(968)	0
Batch normalization 2	(968)	3872
Dropout 1 (Dropout)	(968)	0
Dense 1 (Dense)	(64)	62016
Dropout 2 (Dropout)	(64)	0
Dense 2 (Dense)	(3)	195
Total parameters		**301947**

3.5. Experimental settings

Our experimental work was conducted on a robust computing setup featuring an Intel Core i7-12700F processor paired with 64 GB of RAM. To further enhance computational performance and ensure **reproducibility**, we utilized a GeForce RTX 3070 Ti GPU. For all prior methods, the spatial dimensions were standardized by extracting 3D patches of size 25×25×30. Each patch was processed independently as an image, with the central pixel representing the target mineral class. This approach facilitated the effective learning and extraction of spatial and spectral features.

The dataset was randomly split into three subsets: 70% for training, 10% for validation, and 20% for testing. To ensure a balanced representation of all mineral classes, we selected a total of 4000 samples per class, distributed as follows: 2800 samples for training (70%), 400 samples for validation (10%), and 800 samples for testing (20%). Special care was taken to prevent overlap between image plots across these subsets, ensuring no information leakage between the training and test sets. This precaution was critical to preserving the independence of the test data and preventing any bias in the evaluation process.

Overfitting poses a significant challenge in hyperspectral mineral classification, as it undermines the ability of CNN models to classify unseen data accurately. To mitigate this issue, we implemented

a series of optimization techniques, including batch normalization, L2 regularization, learning rate scheduling, dropout, and K-fold cross-validation. These strategies work synergistically to enhance learning stability and ensure robust generalization, enabling the model to achieve reliable classification performance. The hyperparameters used in this study, detailed in table 3, were fine-tuned based on preliminary experiments to strike a balance between optimal performance and consistent evaluation across methods.

Table 3
Overview of hyperparameter selection in the experimental setup.

Method	Parameter	Value
SAM	Maximum angle (radians)	0.1
2D-CNN	Activation function	ReLU
3D-CNN	Epochs	100
3D-2D-CNN	Batch size	256
	Optimizer	Adam
	Loss function	Categorical crossentropy
	Learning Rate	0.001
	Regularization (L1)	0.006
	Regularization (L2)	0.016
	Momentum	0.99
	Epsilon	0.001
	Dropout	25%
	Learning Rate Decay	10^{-07}
	K-Fold	4

4. Results and discussion

4.1. Evaluation metrics

In this study, we employed various metrics to evaluate the performance of our classification approach. In addition to overall accuracy (OA), we used the Kappa coefficient to assess the agreement between predicted and actual classifications while accounting for chance agreement. We also calculated the average accuracy (AA) to provide class-specific evaluations, highlighting potential performance disparities across different classes [23, 24]. The equations for OA, AA, and the Kappa coefficient are as follows:

$$OA = \frac{TP + TN}{TP + TN + FP + FN} \tag{2}$$

$$AA = \frac{1}{N} \times \sum_{i=0}^{n} \frac{TP_i}{TP_i + FP_i} \tag{3}$$

$$Kappa = \frac{P_0 - P_e}{1 - P_e} \tag{4}$$

Where:

- TP: true positives
- TN: true negatives
- FP: false positives
- FN: false negatives
- P_0: is the observed agreement
- P_e: is the expected agreement by chance

Additionally, the evaluation incorporates F1-score, precision, and recall metrics to provide a more comprehensive understanding of model performance across different dimensions. These metrics are defined as follows:

$$Precision = \frac{TP}{TP + FP} \tag{5}$$

$$Recall = \frac{TP}{TP + FN} \tag{6}$$

$$F1{-}score = \frac{2 \times Precision \times Recall}{Precision + Recall} \tag{7}$$

4.2. Classification results

The classification results obtained for the Djebel Meni region demonstrate the robustness and effectiveness of our approach based on a 3D-2D CNN network. Figure 4 shows the model's training curves, illustrating the evolution of accuracy and loss over 100 training epochs. A maximum accuracy of 99.92% and a minimum loss of 0.0415 was achieved, highlighting the model's exceptional learning ability and instilling confidence in its performance. This performance reflects the model's ability to capture the complex spectral characteristics of minerals while minimizing errors. The stability of the curves, with no signs of divergence, testifies to optimized training supported by techniques such as regularization, dropout, and batch normalization. However, further analysis of test data is crucial to assess the generalizability and robustness of the model in the face of novel data, highlighting the ongoing importance of research in this field.

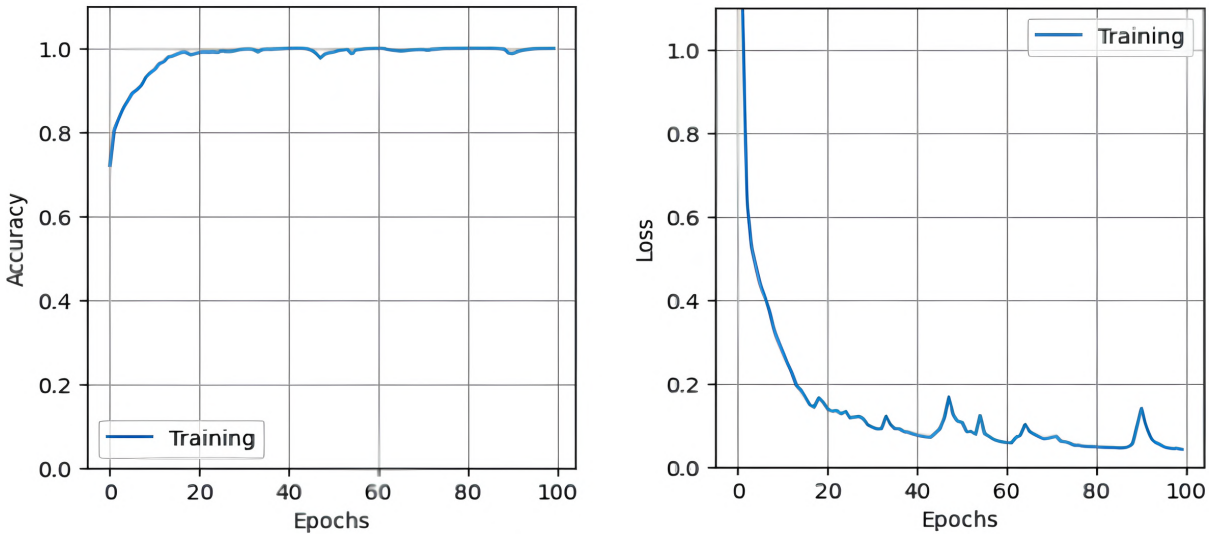

Figure 4: Learning curves.

The results in table 4 highlight the performance metrics of the proposed 3D-2D CNN model for mineral classification in the Djebel Meni region. The average precision 0.94, recall 0.93, and F1-score 0.94 emphasize the model's robustness. Among the classes, Illite achieved the highest scores, with a precision of 0.97, recall of 0.95, and F1-score of 0.96, demonstrating exceptional accuracy in identifying this mineral. Kaolinite and Montmorillonite also showed strong performance, with F1-scores of 0.90 and 0.95, respectively. The overall accuracy of 94.26% and Kappa coefficient 0.9401 indicate high consistency and agreement between predictions and ground truth labels.

The confusion matrix provides further insights into the classification performance. Illite had 758 correctly classified samples, with only 41 misclassifications as Montmorillonite and 1 misclassification as Kaolinite. Kaolinite achieved 729 correct predictions but experienced 71 errors, mostly misclassified

Table 4
Detailed performance metrics and overall results

Classes	Precision	Recall	F1-score
Ilite	0.97	0.95	0.96
Kaolinite	0.89	0.91	0.90
Montmorillonite	0.95	0.94	0.95
Average	**0.94**	**0.93**	**0.94**
Overall accuracy		**0.9426**	
Average accuracy		**0.9393**	
Kappa		**0.9401**	

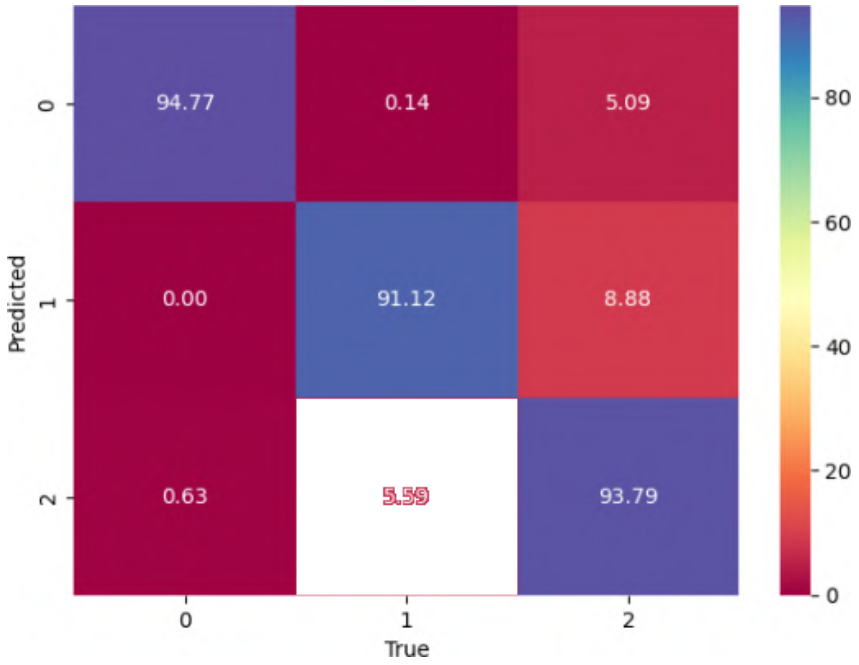

Figure 5: Confusion matrix for our 3D-2D CNN.

as Montmorillonite. Montmorillonite had 750 correctly predicted samples, with 5 misclassified as Illite and 45 as Kaolinite.

The relatively low number of misclassified samples across all classes demonstrates the effectiveness of the proposed model in minimizing errors. However, the higher confusion between Kaolinite and Montmorillonite (71 and 45 errors) suggests overlapping spectral characteristics that require additional features or improved preprocessing to distinguish.

The applied optimization strategies, including dropout, L2 regularization, and batch normalization, effectively reduced overfitting, contributing to the model's strong generalization capabilities. These results confirm the suitability of the 3D-2D CNN model for robust hyperspectral mineral classification, even in complex geological contexts such as the Djebel Meni region.

Table 5 provides a comprehensive comparison of our proposed 3D-2D CNN model with state-of-the-art techniques, including SAM, 2D-CNN, and 3D-CNN, for mineral classification in the Djebel Meni region. The results clearly demonstrate the advantages of our approach, which not only surpasses traditional methods but also addresses key challenges in hyperspectral mineral classification. For the Illite class, our model achieved the highest accuracy (0.9607), significantly outperforming SAM (0.9036), 2D-CNN (0.9345), and 3D-CNN (0.9483). This highlights the model's ability to capture subtle spectral and spatial variations. The Kaolinite class, known for its spectral similarities with other minerals, exhibited a substantial improvement in classification accuracy with our method (0.9054), compared to SAM (0.8543) and even 3D-CNN (0.8963). This improvement underlines the effectiveness of the hybrid

Table 5
Performance comparison of our 3D-2D CNN with state-of-the-art.

Class name	SAM	2D-CNN	3D-CNN	Our method
Ilite	0.9036	0.9345	0.9483	**0.9607**
Kaolinite	0.8543	0.8778	0.8963	**0.9054**
Montmorillonite	0.9087	0.9237	0.9403	**0.9517**
AA	0.8957	0.9196	0.9312	**0.9426**
OA	0.8889	0.9120	0.9283	**0.9393**

3D-2D CNN architecture in distinguishing closely related mineral classes. For Montmorillonite, our approach achieved an accuracy of 0.9517, outperforming SAM (0.9087) and 2D-CNN (0.9237).Moreover, the overall accuracy (OA) and average accuracy (AA) metrics further validate the superiority of our method. With an OA of 0.9393 and an AA of 0.9426, our model consistently outperformed SAM (0.8889, 0.8957), 2D-CNN (0.9120, 0.9196), and 3D-CNN (0.9283, 0.9312). These results confirm that the integration of 3D and 2D convolutional operations provides a balanced trade-off between spectral and spatial feature extraction, enabling enhanced classification performance.

In contrast to previous methods that rely on traditional machine learning models or standalone 2D/3D CNN architectures, our approach introduces a novel hybrid architecture specifically optimized for hyperspectral data. This innovation allows our model to overcome the limitations of earlier techniques, such as their inability to fully exploit the multidimensional nature of hyperspectral data. Additionally, by extending the application of 3D-2D CNNs to mineral classification—previously applied predominantly in vegetation studies—our work broadens the scope of hyperspectral imaging research and demonstrates the versatility of this architecture. In conclusion, the proposed method consistently delivers superior performance across all classes and evaluation metrics. These results confirm the robustness and reliability of our approach, offering a powerful and reproducible framework for mineral classification in hyperspectral imaging. By addressing both spectral and spatial complexities, our work sets a new benchmark for hyperspectral mineral mapping and opens new avenues for exploration in geologically complex terrains.

5. Conclusion

This study presented a 3D-2D CNN model for mineral classification using hyperspectral imaging data from NASA's Hyperion EO-1 sensor in the Djebel Meni region. The proposed approach achieved superior performance compared to state-of-the-art methods, with an overall accuracy of 94.26% and robust classification of illite, kaolinite, and montmorillonite. These results underscore the effectiveness of combining spatial and spectral feature extraction for reliable mineral identification in geologically complex terrains. Looking ahead, we are excited about the potential for future exploration of improved CNN architectures to enhance classification accuracy further and address more complex terrains with a greater number of mineral classes.

Declaration on Generative AI: During the preparation of this work, the authors used the following tools:

- **DeepL** for intelligent translation and grammar correction.
- **Grammarly** for grammar checks, spelling correction, and plagiarism detection.
- **ChatGPT-4** for improving writing style, verifying grammar, and ensuring the logical flow of ideas.

No images were generated using AI tools.

After using these tools/services, the authors reviewed and edited the content as needed and takes full responsibility for the publication's content.

References

[1] H. Shirmard, E. Farahbakhsh, R. D. Müller, R. Chandra, A review of machine learning in processing remote sensing data for mineral exploration, Remote Sensing of Environment 268 (2022) 112750. doi:10.1016/j.rse.2021.112750.

[2] S. Hajaj, A. El Harti, A. B. Pour, A. Jellouli, Z. Adiri, M. Hashim, A review on hyperspectral imagery application for lithological mapping and mineral prospecting: Machine learning techniques and future prospects, Remote Sensing Applications: Society and Environment (2024) 101218. doi:10.1016/j.rsase.2024.101218.

[3] L. Zazi, A. Boutaleb, M. S. Guettouche, Identification and mapping of clay minerals in the region of Djebel Meni (Northwestern Algeria) using hyperspectral imaging, EO-1 Hyperion sensor, Arabian Journal of Geosciences 10 (2017) 252. doi:10.1007/s12517-017-3015-z.

[4] A. F. Goetz, V. Srivastava, Mineralogical mapping in the Cuprite mining district, Nevada, in: Proc. of the Airborne Imaging Spectrometer Data Anal. Workshop, 1985. URL: https://ntrs.nasa.gov/citations/19860002152.

[5] F. A. Kruse, J. W. Boardman, J. F. Huntington, Comparison of airborne hyperspectral data and EO-1 Hyperion for mineral mapping, IEEE Transactions on Geoscience and Remote Sensing 41 (2003) 1388–1400. doi:10.1109/TGRS.2003.812908.

[6] T. Magendran, S. Sanjeevi, Hyperion image analysis and linear spectral unmixing to evaluate the grades of iron ores in parts of Noamundi, Eastern India, International Journal of Applied Earth Observation and Geoinformation 26 (2014) 413–426. doi:10.1016/j.jag.2013.09.004.

[7] X. Zhang, P. Li, Lithological mapping from hyperspectral data by improved use of spectral angle mapper, International Journal of Applied Earth Observation and Geoinformation 31 (2014) 95–109. doi:10.1016/j.jag.2014.03.007.

[8] A. Guha, 15 - Mineral exploration using hyperspectral data, in: P. C. Pandey, P. K. Srivastava, H. Balzter, B. Bhattacharya, G. P. Petropoulos (Eds.), Hyperspectral Remote Sensing, Earth Observation, Elsevier, 2020, pp. 293–318. doi:10.1016/B978-0-08-102894-0.00012-7.

[9] Y. Attallah, E. Zigh, A. P. Adda, Optimized 3D-2D CNN for automatic mineral classification in hyperspectral images, Reports on Geodesy and Geoinformatics 118 (2024) 82–91. doi:10.2478/rgg-2024-0017.

[10] Y. Chen, Z. Lin, X. Zhao, G. Wang, Y. Gu, Deep Learning-Based Classification of Hyperspectral Data, IEEE Journal of Selected Topics in Applied Earth Observations and Remote Sensing 7 (2014) 2094–2107. doi:10.1109/JSTARS.2014.2329330.

[11] C.-I. Chang, Spectral information divergence for hyperspectral image analysis, in: IEEE 1999 International Geoscience and Remote Sensing Symposium. IGARSS'99 (Cat. No.99CH36293), volume 1, 1999, pp. 509–511 vol.1. doi:10.1109/IGARSS.1999.773549.

[12] L. S. Bernstein, S. M. Adler-Golden, R. L. Sundberg, R. Y. Levine, T. C. Perkins, A. Berk, A. J. Ratkowski, G. Felde, M. L. Hoke, A new method for atmospheric correction and aerosol optical property retrieval for VIS-SWIR multi- and hyperspectral imaging sensors: QUAC (QUick atmospheric correction), in: Proceedings. 2005 IEEE International Geoscience and Remote Sensing Symposium, 2005. IGARSS '05, volume 5, 2005, pp. 3549–3552. doi:10.1109/IGARSS.2005.1526613.

[13] Z. Mehalli, E. Zigh, A. Loukil, A. Ali Pacha, Hyperspectral Data Preprocessing of the Northwestern Algeria Region, in: M. Ben Ahmed, H.-N. L. Teodorescu, T. Mazri, P. Subashini, A. A. Boudhir (Eds.), Networking, Intelligent Systems and Security, volume 237 of *Smart Innovation, Systems and Technologies*, Springer Singapore, Singapore, 2022, pp. 635–652. doi:10.1007/978-981-16-3637-0_45.

[14] PeakVisor, Djebel Meni, 2025. URL: https://peakvisor.com/peak/djebel-meni.html.

[15] R. O. Green, B. E. Pavri, T. G. Chrien, On-orbit radiometric and spectral calibration characteristics of EO-1 Hyperion derived with an underflight of AVIRIS and in situ measurements at Salar de Arizaro, Argentina, IEEE Transactions on Geoscience and Remote Sensing 41 (2003) 1194–1203. doi:10.1109/TGRS.2003.813204.

[16] W. Sun, Q. Du, Hyperspectral Band Selection: A Review, IEEE Geoscience and Remote Sensing

Magazine 7 (2019) 118–139. doi:10.1109/MGRS.2019.2911100.
[17] M. K. Tripathi, H. Govil, Evaluation of AVIRIS-NG hyperspectral images for mineral identification and mapping, Heliyon 5 (2019) e02931. doi:10.1016/j.heliyon.2019.e02931.
[18] R. F. Kokaly, R. N. Clark, G. A. Swayze, K. E. Livo, T. M. Hoefen, N. C. Pearson, R. A. Wise, W. M. Benzel, H. A. Lowers, R. L. Driscoll, A. J. Klein, USGS Spectral Library Version 7, Technical Report, US Geological Survey, 2017. doi:10.3133/ds1035.
[19] B.-C. Gao, A. F. H. Goetz, Column atmospheric water vapor and vegetation liquid water retrievals from Airborne Imaging Spectrometer data, Journal of Geophysical Research: Atmospheres 95 (1990) 3549–3564. doi:10.1029/JD095iD04p03549.
[20] L. S. Bernstein, S. M. Adler-Golden, X. Jin, B. Gregor, R. L. Sundberg, Quick atmospheric correction (QUAC) code for VNIR-SWIR spectral imagery: Algorithm details, in: 2012 4th Workshop on Hyperspectral Image and Signal Processing: Evolution in Remote Sensing (WHISPERS), 2012, pp. 1–4. doi:10.1109/WHISPERS.2012.6874311.
[21] H. Li, J. Cui, X. Zhang, Y. Han, L. Cao, Dimensionality Reduction and Classification of Hyperspectral Remote Sensing Image Feature Extraction, Remote Sensing 14 (2022) 4579. doi:10.3390/rs14184579.
[22] E. Zhang, X. Zhang, S. Yang, S. Wang, Improving Hyperspectral Image Classification Using Spectral Information Divergence, IEEE Geoscience and Remote Sensing Letters 11 (2014) 249–253. doi:10.1109/LGRS.2013.2255097.
[23] M. L. McHugh, Interrater reliability: the kappa statistic, Biochemia medica 22 (2012) 276–282. URL: https://pubmed.ncbi.nlm.nih.gov/23092060/.
[24] M. Story, R. G. Congalton, Accuracy Assessment: A User's Perspective, Photogrammetric Engineering and remote sensing 52 (1986) 397–399. URL: https://www.asprs.org/wp-content/uploads/pers/1986journal/mar/1986_mar_397-399.pdf.